Statistical Study of Magnetic Nonpotential Measures in Confined and Eruptive Flares

N. Vasantharaju[1] , P. Vemareddy[2] , B. Ravindra[2], and V. H. Doddamani[1]
[1] Department of Physics, Bangalore University, Bengaluru-560 056, India; vrajuap@gmail.com
[2] Indian Institute of Astrophysics, Koramangala, Bengaluru-560 034, India

Abstract

Using *Solar Dynamics Observatory*/Helioseismic and Magnetic Imager vector magnetic field observations, we studied the relation between the degree of magnetic non-potentiality with the observed flare/coronal mass ejection (CME) in active regions (ARs). From a sample of 77 flare/CME cases, we found in general that the degree of non-potentiality is positively correlated with the flare strength and the associated CME speed. Since the magnetic flux in the flare-ribbon area is more related to the reconnection, we trace the strong gradient polarity inversion line (SGPIL) and Schrijver's R value manually along the flare-ribbon extent. Manually detected SGPIL length and R values show higher correlation with the flare strength and CME speed than automatically traced values without flare-ribbon information. This highlights the difficulty of predicting the flare strength and CME speed a priori from the pre-flare magnetograms used in flare prediction models. Although the total potential magnetic energy proxies show a weak positive correlation, the decrease in free energy exhibits a higher correlation (0.56) with the flare strength and CME speed. Moreover, eruptive flares have thresholds of SGPIL length (31 Mm), R value $(1.6 \times 10^{19}\,\mathrm{Mx})$, and free energy decrease $(2 \times 10^{31}\,\mathrm{erg})$ compared to confined flares. In 90% of eruptive flares, the decay-index curve is steeper, reaching $n_{\mathrm{crit}} = 1.5$ within 42 Mm, whereas it is beyond this value in >70% of confined flares. While indicating improved statistics in the predictive capability of AR eruptive behavior with flare-ribbon information, our study provides threshold magnetic properties for a flare to be eruptive.

Key words: Sun: activity – Sun: coronal mass ejections (CMEs) – Sun: flares – Sun: general – Sun: magnetic fields – Sun: photosphere

1. Introduction

Energetic events such as flares and coronal mass ejections (CMEs) generally occur in magnetically concentrated locations called active regions (ARs). It is believed that these events are physically related to the magnetic complexity and non-potentiality of ARs. However, the question of how the magnetic complexity and non-potentiality trigger the flares and CMEs remains unanswered. For this reason, solar flare forecasting models mainly depend on the statistical relationship between flare production and the non-potential magnetic parameters characterizing the AR size, strength, morphology, magnetic topology, etc. Conventionally, the magnetic complexity and non-potentiality are described in terms of parameters such as the magnetic shear (Hagyard & Rabin 1986; Wang et al. 1994a), horizontal gradient of longitudinal magnetic field (Zirin & Wang 1993; Tian et al. 2002), electric current (Leka et al. 1993; Wang et al. 1994b), twist parameter α (Pevtsov et al. 1994; Hagino & Sakurai 2004; Tiwari et al. 2009), magnetic free energy (Metcalf et al. 2005), current helicity (Abramenko et al. 1996; Zhang & Bao 1999), etc. Although individual cases have identified a direct role of these non-potential parameters in the observed activity (Vemareddy et al. 2012), their relationship is not quite strong enough in statistically significant samples of flares/CMEs, and hence is inadequate for the prediction of space weather.

Past observational studies have explored the connection between photospheric magnetic fields and solar flares, supporting the claim that the latter are driven by the non-potentiality of magnetic fields in ARs (Leka et al. 1993; Wang et al. 1994b, 1996; Tian et al. 2002; Abramenko 2005). Several observations have revealed that solar flares often occur near polarity inversion lines (PILs) with a high gradient of longitudinal magnetic field and/or strong shear of transverse components (Hagyard et al. 1990; Wang et al. 1994a; Falconer et al. 1997; Kosovichev & Zharkova 2001; Jing et al. 2006; Schrijver 2007). Because of this, the magnetic shear, magnetic gradient, and vertical electric currents in the photosphere are the most commonly used measures of magnetic non-potentiality.

Both gradient and shear have been employed as parameters in solar activity forecast models. For example, in a sample of 17 vector magnetograms, Falconer (2001) and Falconer et al. (2003) measured the lengths of strong-sheared and strong-gradient magnetic neutral line segments, respectively. Their study found that strong-sheared, strong-gradient PIL (SGPIL) segments are strongly correlated with each other, suggesting them to be prospective predictors of the CME productivity of ARs. Leka & Barnes (2003a, 2003b) investigated the magnitudes and temporal variations of several photospheric magnetic parameters in three ARs. They demonstrated that individually these parameters have little ability to differentiate between flare-producing and flare-quiet regions, but in certain combinations, two populations may be distinguished. Song et al. (2006) showed that the SGPIL is a viable tool to locate source regions of either CMEs or flares. The definitive flare/CME predictive ability by measuring SGPILs is about 75% (55 out of 73 events). Based on a study of 298 ARs, Georgoulis & Rust (2007) argued that a connected magnetic field is a robust metric to distinguish X- and M-flaring regions from non-flaring ones. A further study by Song et al. (2009) proved that the SGPIL is the most promising parameter in determining solar flares, if only one parameter can be chosen. In combination with PIL length, total unsigned flux, and effective separation, Mason & Hoeksema (2010) introduced the gradient-weighted PIL length as a characteristic for solar flare forecasting; however, the skill score test still indicates it is not a reliable

parameter for real-time prediction of flares. However, Sadykov & Kosovichev (2017) demonstrated the importance of PIL characteristics in solar flare forecasts.

Knowledge of the amount of magnetic free energy and its temporal variation associated with flares/CMEs is important in understanding the energy storage and release processes in ARs. The deviation from potential energy is taken as a proxy for magnetic free energy. Leka & Barnes (2007) considered the total excess energy as one of the best performing parameters. Emslie et al. (2012) demonstrated for a sample of 38 flares that the total magnetic free energy was sufficient to explain the flare energy release including CMEs, energetic particles, and hot plasma emission and dynamics. Studies on the correlation between magnetic free energy estimated from three-dimensional, nonlinear force-free fields (3D NLFFFs) and flare index confirm the physical link between them (Jing et al. 2010). Su et al. (2014) showed that in flaring ARs, the 3D NLFFF magnetic free energy and that obtained from photospheric magnetic fields have almost equal predictability for flares.

Motivated by the above studies, we further investigated the relationship between the non-potentiality of magnetic fields in statistically significant source ARs and the observed flare/CME productivity using vector magnetograms. The focus of this study seeks to address the question of whether the degree of non-potentiality has any correspondence with the magnitude of the flares and the speed of the CMEs. Both flares and CMEs are magnetically driven phenomena of stored magnetic energy configurations, and it is of great importance to distinguish the AR conditions that produce flares and that lead to a flare becoming eruptive, successfully ejecting material as a CME. Note that coronal rain is also a kind of eruption but fails to eject material. Seeking such a link of AR non-potential parameters, first to flares and then to CMEs, involves a careful manual inspection of which CME comes from which AR and the availability of vector magnetic field measurements within $\pm40°$ of the disk center. Therefore, our study is limited in sample size compared to several studies based on line-of-sight magnetograms as stated above. In Section 2, we give a brief description of the observational data and the procedures used to calculate the various magnetic field parameters. The results of non-potential measurements and their relation to flares and CMEs are discussed in Section 3. A summary and discussion are presented in Section 4.

2. Observational Data and Analysis

The required vector magnetic field observations are obtained from the Helioseismic and Magnetic Imager (HMI; Schou et al. 2012) aboard the *Solar Dynamics Observatory* (*SDO*). For ready use in AR analysis, the HMI provides processed space-weather HMI AR patches at 720 s cadence. This data product contains field components (B_r, B_θ, B_ϕ) in a spherical coordinate system after the heliographic cylindrical equal area projection (Calabretta & Greisen 2002) centered on the AR patch. These components are equivalent to (B_z, $-B_y$, B_x) in a Cartesian system. More information on the HMI data pipeline and the field transformation is given in Hoeksema et al. (2014), Sun (2013). The data on CME linear speed, flare initiation, and end timings were obtained from the relevant websites: https://cdaw.gsfc. nasa.gov/CME_list/ (Gopalswamy et al. 2009); https://www. spaceweatherlive.com/en/archive, http://xrt.cfa.harvard.edu/ flare_catalog/all.html. For a statistically significant inference,

we considered 77 flare events during the period from 2011 February to 2016 July and their source ARs were located within $40°$ of the central meridian to minimize projection effects on the calculation of magnetic properties. Their heliographic locations are shown in Figure 1. We also excluded flares from inter-ARs (Toriumi et al. 2017) and/or not associated with PILs. Thus, our sample constitutes 14 X-class, 42 M-class, and 21 C-class flares. Among the sample, 38 flares are associated with CMEs visible at least in the LASCO C2 field of view. The procedures for the derivation of various magnetic parameters are described in the following subsections.

2.1. Strong Gradient and Strong Sheared PIL Length

PILs mark the separation between positive and negative magnetic flux patches in the photosphere of ARs. Solar flares generally occur in the strong magnetic regions with SGPILs, or in complex polarity patterns. Several researchers have measured the PIL length and studied its relationship with flare productivity (Falconer et al. 2003; Jing et al. 2006; Song et al. 2006; Bokenkamp 2007; Schrijver 2007; Mason & Hoeksema 2010). Bokenkamp (2007) developed a three-step iterative algorithm to measure the gradient-weighted PIL lengths, originally based on the Falconer et al. (2003) method. In the first step, zero Gauss contours are identified in the strongly smoothed line-of-sight magnetic field (B_{los}) map, and the vector magnetic field map is calculated from the smoothed B_{los} using a linear force-free field model (Alissandrakis 1981). From the output of this step, PIL segments are identified as zero Gauss contours with specific thresholds of simulated potential transverse field and horizontal gradient of B_{los}. In the second step, the above process is repeated for the less smoothed B_{los} image and the output PIL segments are identified by comparing those obtained using this step and the previous one. Finally, in the third step, the same process is repeated for the unsmoothed B_{los} and the gradient-weighted PIL length is obtained by comparing the segment outputs from this step and the previous one. Here we employed a single-step algorithm to measure the SGPIL and strong shear PIL (SSPIL) lengths based on Bokenkamp's algorithm. These PILs are defined in the following paragraphs.

The non-potential nature of the magnetic field is characterized by magnetic shear as the difference between the directions of observed ($\boldsymbol{B}_o$) and potential ($\boldsymbol{B}_p$) transverse fields, and is given by $\theta = cos^{-1}(\boldsymbol{B}_o \cdot \boldsymbol{B}_p/|\boldsymbol{B}_o\boldsymbol{B}_p|)$ (Ambastha et al. 1993; Wang et al. 1994a). The PIL segment on which the observed transverse field has a strength above the threshold value of 150G and the magnetic shear angle has a value exceeding $45°$ is marked as an SSPIL (Falconer et al. 2003; Vemareddy et al. 2015). We measured the SSPILs both automatically ($SSPIL_A$) and manually ($SSPIL_M$). Our algorithm (automatic) identifies multiple strong shear PILs in an AR and the sum of these PIL lengths gives $SSPIL_A$. In this procedure, we smooth the vertical magnetic field (B_r) image to a smoothing factor of 8 pixels (4 arcsec) and identified the zero Gauss contour. Then the potential magnetic field is calculated from the strongly smoothed magnetogram and the shear map is generated from the computed potential and the observed transverse field. On applying the thresholds of the strong observed transverse field, B_t (>300 G) and strong shear angle ($>45°$) to contour segments, the strong field and strong shear PILs are identified. The summation of these PIL lengths gives $SSPIL_A$.
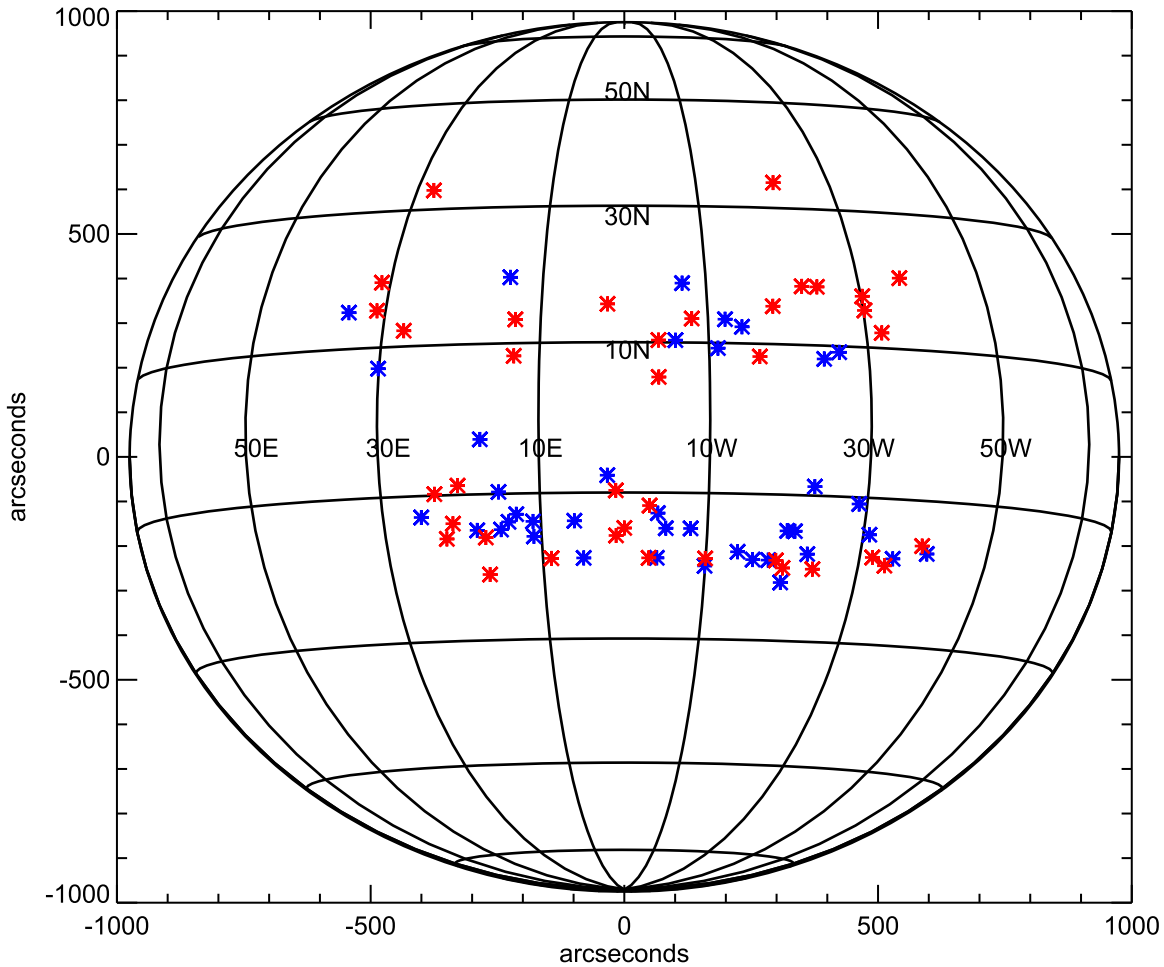
Figure 1. Heliographic locations of all 77 events used in the study. Red (blue) asterisk symbols represent eruptive (confined) flares.

In the case where vector magnetograms are not available, the shear information is alternatively obtained using horizontal gradients in line-of-sight magnetograms where the SGPIL serves the purpose of the SSPIL (Falconer et al. 2003). In this procedure (automatic), we identify the zero Gauss contours on the smoothed magnetogram. The potential magnetic field and vertical magnetic field gradient maps are generated by the strongly smoothed magnetogram. Using thresholds of potential transverse field ($>300\,\text{G}$) and high vertical magnetic field gradient ($>50\,\text{G/Mm}$) to the zero Gauss contour segments, $SGPIL_A$ is determined.

To illustrate this procedure, we display AR NOAA 11429 in Figure 2. Panel 2(a) shows flare ribbons in the AIA 1600 Å snapshot taken during the *GOES* soft X-ray peak time (2012-03-07 00:24 UT) of flare X5.4 from AR 11429. The flare brightening region indicates the site of flare occurrence. These flare ribbons generally trace the SGPIL/SSPIL with some departures as displayed in the overplotted Bz map (Figure 2). In panel 2(c), we trace automatically $SGPIL_A$ marked by the blue curve on the gradient map of Bz. This difference slightly increases depending on the complexity of the AR. It can be noticed that both $SGPIL_A$ and $SSPIL_A$ trace the same segments of the PIL and measure the length with a slight difference. A similar trace is obtained with $SSPIL_A$ as shown in shear map of panel 2(d). $SSPIL_A$ also follows the flare brightening region to a large extent with differences at the middle. In panel 2(e), we

overplot $SGPIL_A$ (blue curve) on Bz map and $SSPIL_A$ (blue) is overlaid on the vector magnetogram in panel 2(f).

Owing to differences in the automatically traced SGPIL/SSPILs with the actual extent of flare ribbons during peak time, we undertook an experiment by following these PIL segments manually with the flare ribbon information. Unlike the automated procedure, the manual tracing is biased by the flare brightening area which overlaps with the SSPIL/SGPIL. In this way, we extract only the strong shear/gradient PIL segment that mostly contributes to the flare brightening. The underlying idea to invoke information about the flare brightening is that the flux along the extent of the flare ribbon contributes to strength of the flare but not all PIL segments with strong shear/gradient contribute to the flare intensity. We denote the total length of all these manually traced segments as $SSPIL_M$ and $SGPIL_M$. In the future, this manual method could be easily automated (for a few cases) by applying brightness thresholds to AIA 1600 Å images and use these as a mask for HMI magnetograms. However, we are constrained to manually trace these PILs at the peak phase of the flare and verify the extent of the ribbons along the PIL. This procedure is subject to human error and may not reproduce the same values.

2.2. Magnetic Flux

The total absolute flux in the AR is computed using $\Phi = \Sigma |B_z| dA$, where dA is the area of an observation pixel.
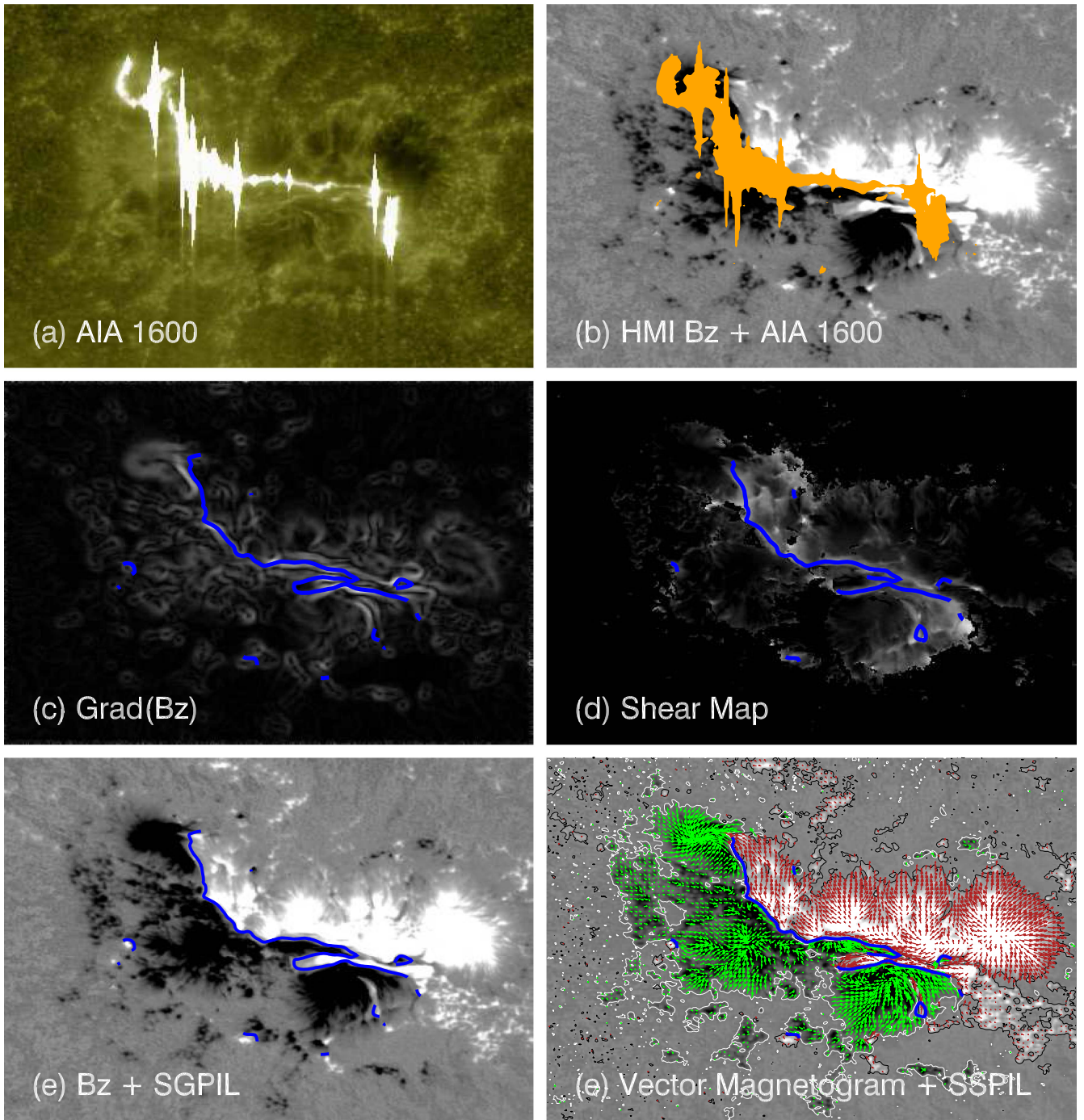
Figure 2. Tracing SSPIL$_A$ and SGPIL$_A$ in AR 11429 on 2012 March 7. (a) AIA 1600 Å image with flare brightening corresponding to the peak time of the X5.4 flare; (b) HMI photospheric magnetogram Bz with filled contours of the AIA 1600 Å flare brightening (orange patch) overplotted; (c) automatically traced SGPIL$_A$ (blue curve) overplotted on the Bz gradient map; (d) automatically traced SSPIL$_A$ overplotted on the magnetic shear map; (e) SGPIL$_A$ overplotted on the Bz map; (f) vector magnetogram with horizontal magnetic field vectors (red and green arrows) overplotted on the Bz map. SSPIL$_A$ is shown as a blue curve. It is noted that the flare brightening generally traces SGPIL/SSPIL with differences (at the middle) increasingly in more complex ARs.

The emergence of electric current embedded in the magnetic flux plays a main role in triggering the flares (Leka et al. 1996; Schrijver et al. 2005; Vemareddy et al. 2015). As the SGPIL is the proxy for such emerging photospheric electric currents, the flux near the SGPILs, defined by R, must have a strong relation with the flares as first proposed by Schrijver (2007). Following the procedure prescribed by Schrijver, we constructed binary maps of positive and negative strong-field masks with threshold values of

$+300\,\mathrm{G}$ and $-300\,\mathrm{G}$ respectively (Guerra et al. 2018); these maps were then dilated by a 6×6 square pixel kernel to create dilated positive and negative bitmaps. The regions of overlap of these two bitmaps were identified as PILs. The region of overlap was convolved with normalized Gaussian of FWHM 15 Mm to create the weighting map. Finally, this weighting map was multiplied by the absolute value of the magnetogram (B_z), and the weighted unsigned flux density integrated over all pixels gave the value of
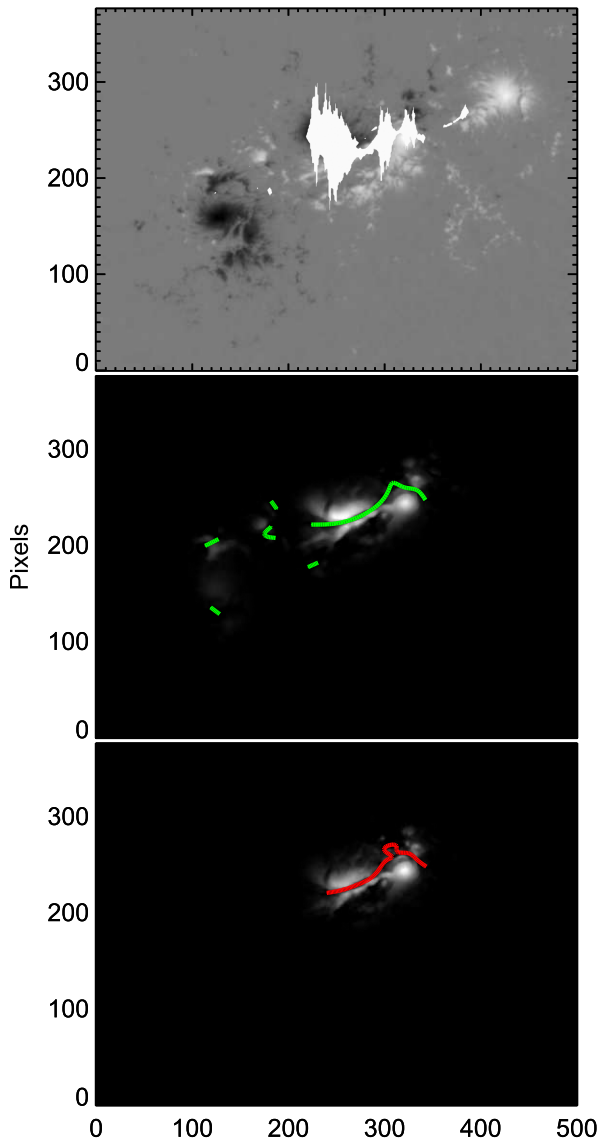
Figure 3. Top: HMI magnetogram B_z map of AR 11158 obtained on 2011 February 15 during the X2.2 flare. Contours of the AIA 1600 Å flare brightening at flare peak time (01:45 UT) are overplotted. The unsigned flux density B_z summed over all pixels gives Φ. Middle: magnetogram B_z multiplied by the weighted map of the field near $SGPIL_A$ (green curves). Summing the absolute values of B_z at these pixels yields R. Bottom: magnetogram B_z multiplied by the weighted map of the field near $SGPIL_M$ (red curve). Summing the absolute values of B_z at these pixels gives R_{SG}.

R. R_{SG} was measured similarly along the $SGPIL_M$ segments. Note that R and R_{SG} differ in flare brightening information. One such example is shown in Figure 3.

2.3. Magnetic Energy

The total energy in the coronal field is estimated using a virial theorem equation provided by magnetic field observations at the photospheric surface (Chandrasekhar 1961; Molodensky 1974; Low 1982) and is given by

$$E = \frac{1}{4\pi} \int_S (xB_x + yB_y)B_z\,dx\,dy. \tag{1}$$

The use of this equation at the solar photosphere is restricted because the photosphere field is not fully force-free and not precisely flux-balanced in a finite area surrounding the AR of

interest. Therefore, the photospheric energy estimate serves only as proxy for the energy content in the AR magnetic structure. The potential magnetic fields are derived from the B_z component using the Fourier transform method (Gary 1989). Since the potential field state is a minimum energy state, by subtracting the potential energy (E_p) from the total energy (E) one obtains the upper limit of the free energy (E_f) available in the AR to account for energetic events likes flares and CMEs.

2.4. Decay Index of the Coronal Background Field

The coronal magnetic field gradient is referred to as the decay index $n(z)$, considered an important parameter in controlling the eruptiveness of an AR. In flux-rope-based CME models (Török & Kliem 2005; Olmedo & Zhang 2010; Cheng et al. 2011), if the decay index of the overlying magnetic field reaches a critical value, then it results in torus instability (rapid decay of the overlying magnetic fields), which leads to CME eruption.

The decay index is defined as $n(z) = -\frac{z}{B_h}\frac{\partial B_h}{\partial z}$, where z is the geometrical height from the bottom boundary (photosphere) and $B_h(=\sqrt{B_x^2 + B_y^2})$ is the horizontal field strength. We compute the background field in the entire volume of AR magnetic structure by the potential field approximation (Gary 1989) using the observed vertical component of the magnetic field at the photosphere. From this extrapolated field, B_h as a function of height is obtained at eight points along the main PIL and an average of $n(z)$ is then derived. Török & Kliem (2005) proposed a constant value of 1.5 as a critical decay index (n_{crit}), which is a subjective value based on different conditions. The height at which the n-curve reaches an n_{crit} of 1.5 is considered the critical height. We estimate this critical height for all the events in our sample.

3. Results

3.1. PIL Length versus Flare Strength

High vertical field gradients and strong shear usually appear in the vicinities of PILs, where flares frequently occur (Hagyard & Rabin 1986; Hagyard 1988; Falconer et al. 2003; Sharykin et al. 2017). Following the procedure described in Section 2.1, we estimated the lengths of both the SSPIL and SGPIL for all the sample flaring ARs called $SSPIL_A$ and $SGPIL_A$ (automatically) and $SSPIL_M$ and $SGPIL_M$ (manually). In this regard, we used vector magnetograms available immediately before the initiation time of the flares. In Figures 4(a) and (b), we show the relationship of $SSPIL_A$ and $SGPIL_A$ with flare strength. As our algorithm identifies, multiple PIL segments of high gradient and strong shear in an AR and their summation $SGPIL_A$ and $SSPIL_A$ respectively show a weak correlation with flare strength at a Spearman's rank correlation coefficient of ∼0.4. As we are keen to find the correlation between flare strength and the PIL segment of high gradient and strong shear in the flare brightening region, we traced $SGPIL_M$ and $SSPIL_M$ manually as described in Section 2.1.

Here and in the following, linear regression analysis is done using the FITEXY.PRO routine available in the SolarSoftWare library, where it uses a least-squares approximation in one dimension to fit the best straight line to the data with errors in both coordinates. We used the standard deviations of both coordinates as error inputs. The uncertainties in both the obtained coefficients are shown in the equation, inserted in the figure panels. We estimated the Spearman ranking correlation
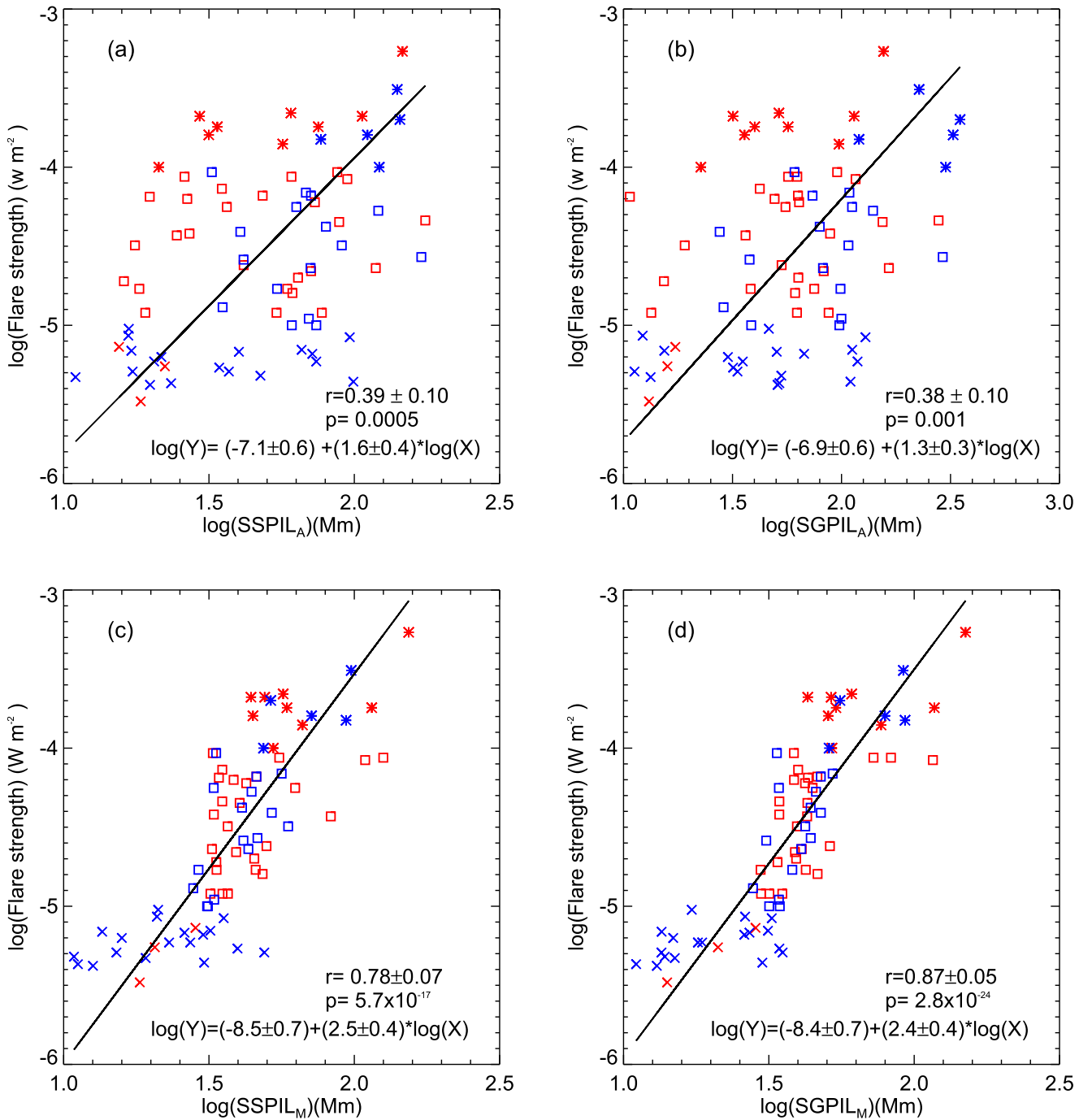
Figure 4. Top two panels: scatter plots of automatically detected $SSPIL_A$ and $SGPIL_A$ with flare strength; bottom two panels: scatter plots of manually detected $SSPIL_M$ and $SGPIL_M$. Spearman ranking correlation coefficient (r), two sided significance (p-value), and the equation of the solid fitted line are inserted in each panel. The crosses, squares, and asterisks represent the C-class, M-class, and X-class flares respectively. The red (blue) color of these symbols corresponds to eruptive (confined) flares. Note that the manual detection method implies a higher correlation with flare strength.

coefficients (r) in all our studies and the standard error in r was estimated by $ERR_r = \sqrt{((1 - r^2)/(n - 2))}$. From here onwards, we refer to Spearman ranking correlation coefficient as CC.

In Figures 4(c) and (d), $SGPIL_M$ and $SSPIL_M$ are plotted against flare strength, respectively. It can be seen that the length of both $SGPIL_M$ and $SSPIL_M$ increases with flare strength. This indicates that more intense flares tend to occur from ARs having larger PILs weighted by strong vertical field gradients, a proxy for strong shear. ARs with large PILs are indicative of a complex field structure, and PILs with large gradients are

indicative of shearing. Therefore, the SGPIL and SSPIL both describe the global non-potentiality of ARs. $SGPIL_M$ has a better correlation with flare strength at a CC of 0.87 than that of $SSPIL_M$ with flare strength at a CC of 0.78. These strong correlations with flare strength confirm that the flare productivity depends on the non-potentiality of ARs. Importantly, it is noted that 35 out of the 38 CME associated cases (red symbols) have an SGPIL length larger than the threshold of $Log10(SGPIL) = 1.5$ (31 Mm). This may indicate that CME occurrence requires a certain minimum SGPIL length to be eruptive from a confined environment.
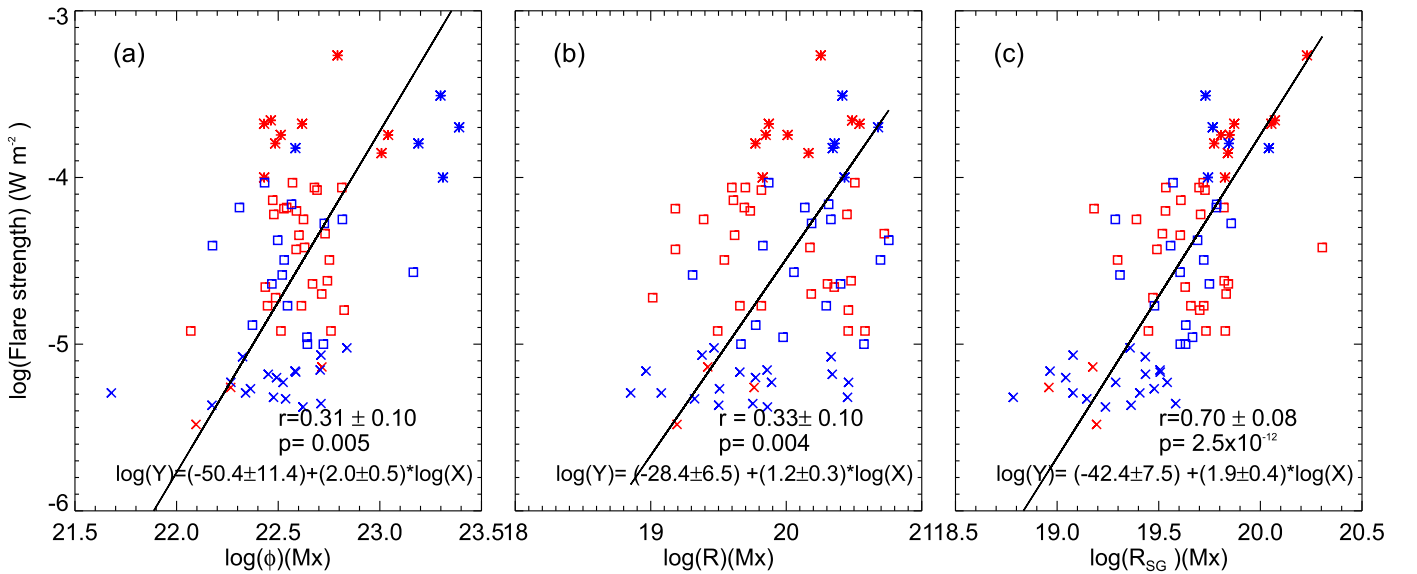
Figure 5. Scatter plots of Φ, R, and R_{SG} with flare strength in the left, middle, and right panels, respectively. Spearman ranking correlation coefficient, two-sided significance (p-value), and the equation of the solid fitted line are inserted in each plot. The crosses, squares, and asterisks represent the C-class, M-class, and X-class flares respectively. The red (blue) color of these symbols corresponds to eruptive (confined) flares.

Table 1
Contingency Table Based on $SGPIL_M$ Length for the Forecast of CMEs

No. of samples	CME occurrences	Non-CME occurrences	Total
Log($SGPIL_M$) $\geqslant$ 1.5 (yes)	35 (H)	22 (FA)	57
Log($SGPIL_M$) < 1.5 (No)	3 (M)	17 (CN)	20
Total	38	39	77

The above relation is tested for statistical significance. We construct a contingency table for Log($SGPIL_M$) $\geqslant$ 1.5 and CME productivity from all the flaring ARs (both confined and eruptive) in our sample, and this is shown in Table 1. Fisher's exact test is applied to check for the significance of the relationship between these two variables. The p-value is determined using a hypergeometric distribution and is found to be 2.9×10^{-4}, which is statistically significant. This relation is not significant for $SGPIL_A$, since we can see there is no clear threshold value for distinguishing the confined and eruptive flares. Further, this threshold value of $SGPIL_M$ is used as a forecasting parameter for CME productivity. Forecast verification measures like the True Skill Statistic (TSS) and Heidke Skill Score (HSS) were calculated using the forecast contingency table (Bloomfield et al. 2012) as shown in Table 1. Both of these measures account for correct random forecasts and can have a range of skill scores from -1 to $+1$. TSS and HSS were found to be 0.357 and 0.355 respectively.

Further, the estimated length of $SSPIL_M$ was plotted against that of $SGPIL_M$ (plot not shown). They are highly correlated at a CC of 0.92. Our result in a large sample is consistent with that of Wang et al. (2006), who showed a strong correlation between magnetic gradient and magnetic shear in primary PILs of five strong flaring ARs. This high correlation is not a surprise as Falconer et al. (2003) already indicated that the SGPIL is a viable proxy for the SSPIL and it is well correlated with the CME productivity of ARs. As the SGPIL can be measured from the line-of-sight magnetogram, it serves as a substitute for the SSPIL in CME/flare forecasting studies.

3.2. Total Unsigned Flux, Magnetic Energy versus Flare Strength

In the past many studies were conducted on the association of flares and the flux content of ARs (Leka & Barnes 2003a, 2003b; Schrijver 2007; Bobra & Couvidat 2015; Kazachenko et al. 2017). They commonly found a weak correlation between total unsigned flux of the whole AR with flare strength. Recently, Kazachenko et al. (2017) found a strong correlation between the reconnection flux, i.e., the total unsigned flux of the flare ribbon area, with flare strength. Along the same lines, we conducted three different studies to find the relationship between flares and the total unsigned flux quantitatively: first, the total unsigned flux (Φ) of the whole AR; second, Schrijver's R value, which is the total unsigned flux within 15 Mm of all SGPILs in the AR; third, R_{SG} (similar to the flare ribbon reconnection flux as defined in Kazachenko et al. 2017), which is the total unsigned flux within 15 Mm of $SGPIL_M$ but only the flare ribbon extent.

In Figure 5(a), the total unsigned flux from the whole AR is plotted against flare strength and shows a weak correlation of CC $\sim$ 0.31. In Figure 5(b), R is plotted against flare strength and also shows a weak positive correlation of CC = $\sim$0.33. In Figure 5(c), R_{SG}, the flux from the flare eruption site, has a strong association with flare strength of CC $\sim$0.70. These results indicate that the flux near $SGPIL_M$ has a strong connection to the flare strength. This suggests that flare strength depends neither on the total unsigned flux of whole AR (as it just represents the size of the AR) nor on the flux near all the SGPILs in an AR, but there is a strong physical dependence with flux from the region of 15 Mm around $SGPIL_M$ which overlaps the flare brightening. This result also confirms that of Kazachenko et al. (2017) and may be more robust given better statistics. This refined relation points to the difficulty of predicting the flare and its strength based on pre-flare magnetograms.

We explore the relationship between magnetic energy and flare strength in Figure 6. The total magnetic energy for all flare events in our sample at the initial and end timings of the flares was estimated (Section 2.3). The total magnetic energy and
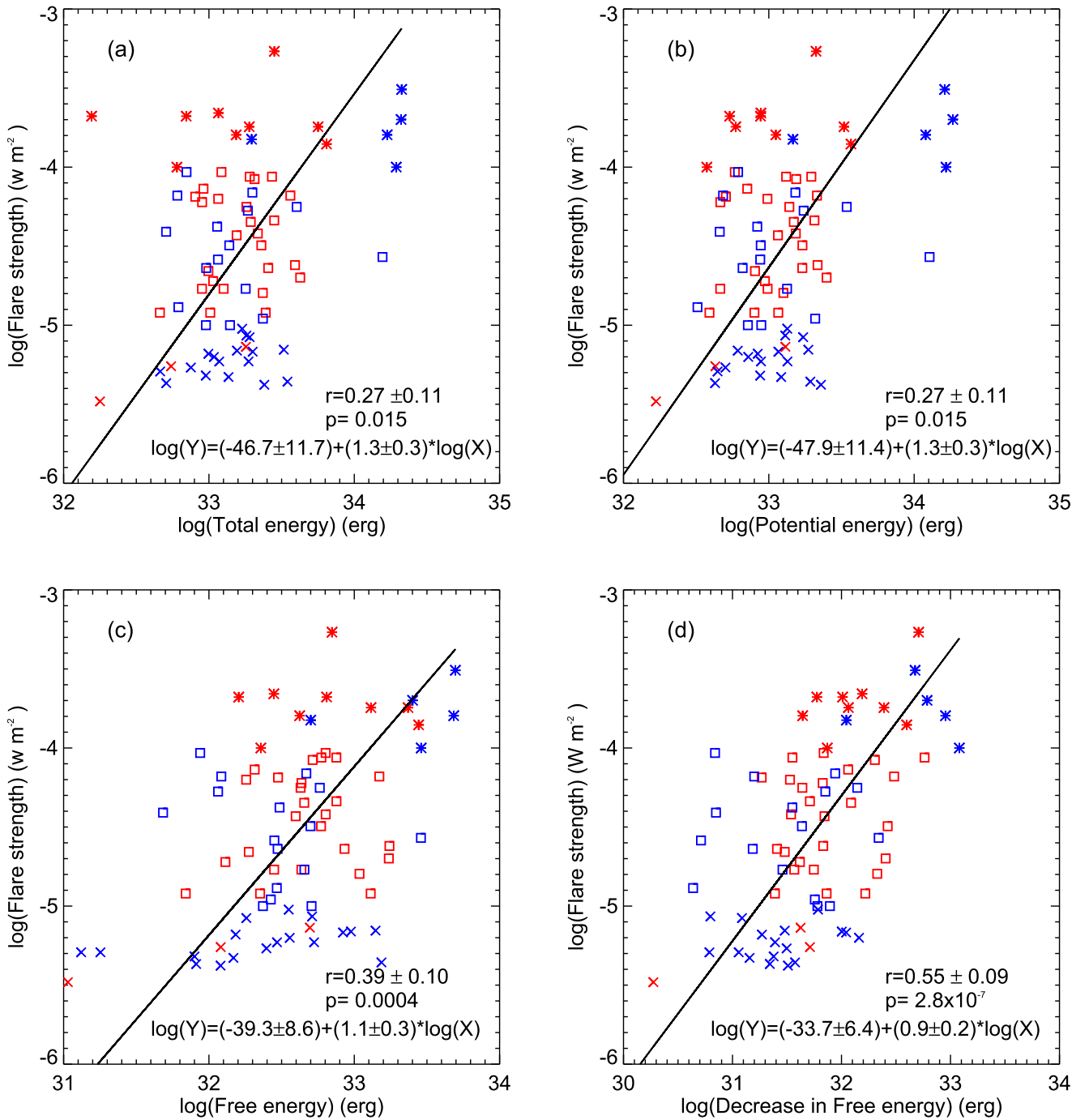
Figure 6. Scatter plots of (a) total magnetic energy, (b) potential energy, (c) free energy, (d) decrease in magnetic free energy, against flare strength in logarithmic scale. Spearman ranking correlation coefficient, two sided significance (*p*-value), and the equation of the solid fitted line are inserted in each panel. The crosses, squares, and asterisks represent the C-class, M-class, and X-class flares respectively. The red (blue) colors of these symbols corresponds to eruptive (confined) flares. Note the higher correlation of decrease in free energy with flare strength.

potential energy at the initial times are each weakly correlated with flare strength with a CC of 0.27 as shown in panels 6(a) and (b). In panel 6(c), the magnetic free energy is plotted against flare strength. Despite the points being scattered, there is a moderate positive correlation with a CC of 0.39.

Over our whole sample, the magnetic free energy estimated at flare end timings is found to be smaller than that estimated at the initial timings. Panel 6(d) depicts the correlation between the decrease in free energy with flare strength. Unlike the energy estimates at initial times, the scatter plot shows a

moderate positive correlation (CC = 0.55), indicating a physical link between the decrease in free magnetic energy and the intensity of flares. This indicates that the total amount of magnetic energy and potential energy possessed by an AR has very little to do with the intensity of flares that the AR has produced, but the difference in total magnetic free energy before/after the flare is directly proportional to its strength, as one would expect. This result is corroborated by the strong correlation between flare strength and the amount of free energy decreased during the flares (Vemareddy et al. 2012),
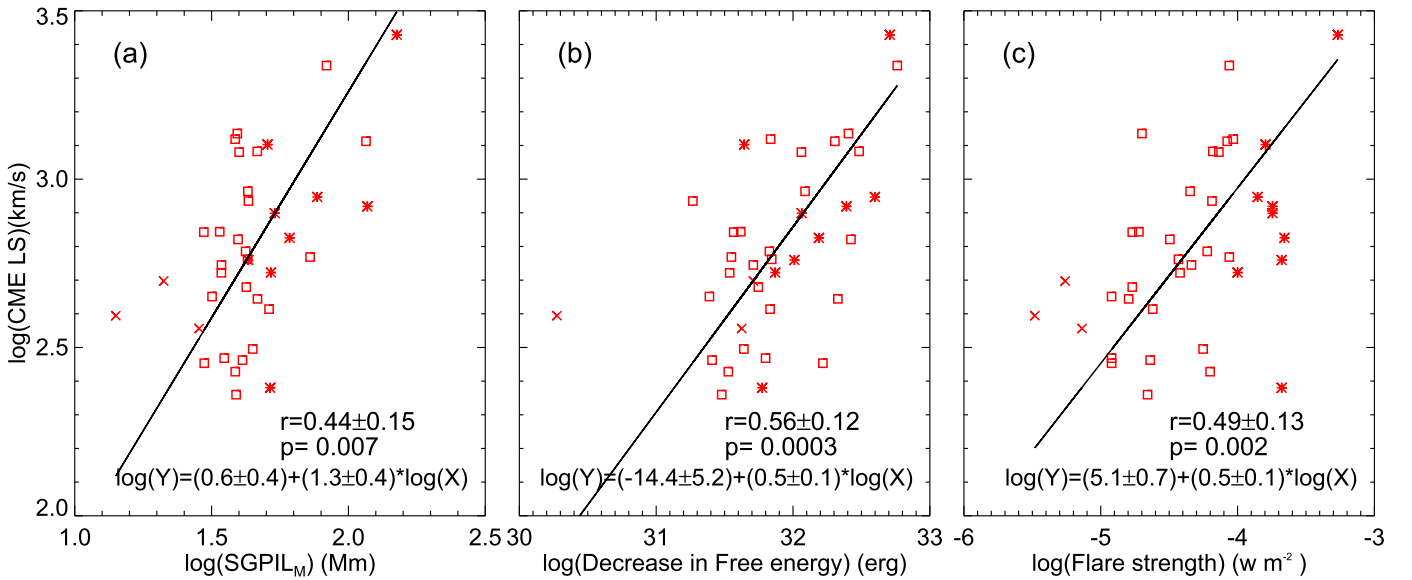
Figure 7. Relation of CME kinematics with AR magnetic properties. The scatter plots of (a) $SGPIL_M$, (b) decrease in free energy and (c) flare strength with CME speed. Spearman ranking correlation coefficient, two-sided significance (p-value), and the equation of the solid fitted line are inserted in each plot.

and hence it is clearly evident that the larger the amount of energy released, stronger the erupted flares. Notably, the free energy decrease for the CME cases (35 of 38, red symbols) starts from 2×10^{31} erg (Log(31.3)) and may indicate the threshold energy required for a flare to be eruptive.

3.3. Magnetic Properties of the Active Region versus CME Kinematics

From the sample of 77, 38 flares are CME associated (eruptive flares) and have known source ARs. We used the online LASCO/CME catalog to determine the CME/flare association and linear speed of the CMEs. The relationship between these 38 source AR properties and the associated CME speeds are examined in Figure 7. The observed CME speed follows a positive correlation with $SSPIL_M$ and $SGPIL_M$ with CCs of 0.43 and 0.44 respectively. For reference, only the plot of $SGPIL_M$ versus CME linear speed is displayed. This implies that faster CMEs tend to initiate in ARs with longer PIL lengths surrounded by greater magnetic complexity (Falconer et al. 2003; Song et al. 2006).

There is a reasonably high positive correlation between the decrease in magnetic free energy after the flare eruption and CME linear speed (panel 7(b)) with a CC of 0.56. We explored the relationship between magnetic free energy before the flare eruption and CME linear speed as well, but the correlation is weak (plot not shown). As the decrease in free energy involves the difference ($FE_{initial} - FE_{end}$), it correlates well with CME speed. Further, we also studied the relationship between the total unsigned flux with CME linear speed but found a weak correlation between them (plot not shown). These results suggest that there is a strong physical link between the released non-potential energy of the source AR and CME speed but there is no evidence that CME kinematics depends on the size of the AR. This result is in accord with previous studies that were done using line-of-sight magnetograms (Chen et al. 2011). The latter authors claimed that the size, strength, and complexity of ARs have little to do with the kinematic properties of CMEs, but have a significant effect on CME productivity.

Flare strength and CME speed are also positively correlated with a CC of 0.49, shown in panel 7(c). This suggests a general relation that CME speeds are proportional to flare strength and would underpin the action of impulsive reconnection on the expelled CME, in agreement with previous studies (Guo et al. 2007; Wang & Zhang 2007), although there have been a few recently found exceptions (e.g., Sun et al. 2015).

3.4. Confined and Eruptive Flares

In this section, we investigate the role of the background coronal field in confined flares (without CMEs) and eruptive flares (associated with CMEs). Following the procedure described in Section 2.4, we estimated the critical decay index heights for all 77 events in our sample. In Figure 8, $n(z)$ is plotted for typical cases of eruptive (left column) and confined (right column) flares. B_h (average of eight points along the main PIL) as a function of height is also shown in each panel. For eruptive flares, the extrapolated field reaches this critical value at a height below 45 Mm. Notably, at about 10 Mm the curve exhibits a gradual steepness with a "bump" in the eruptive cases and is missing in the confined cases with an almost smooth curve. The bump is also found in the Cheng et al. (2011) study and is interpreted as a distinct shape for eruptive and non-eruptive flare events. It is noticed that B_h decreases faster in the low corona (about 10 Mm), and the appearance of a bump in the eruptive flare cases may indicate the ability of the twisted flux (flux rope) to experience torus instability. From these panels, it is seen that the $n(z)$ curve is steeper, reaching $n_{crit} = 1.5$ within 40 Mm for the eruptive cases. For the confined flares, the $n(z)$ gradually reaches n_{crit} well beyond a height of 50 Mm.

In Figure 9, we plot the critical heights of all events versus flare strength. It can be seen that the both the confined (blue circles) and eruptive (red circles) flares spread all along the height n_{crit} and have no relation to the flare strength. Further, (Liu 2008) proposed a typical height of eruption onset of 42 ± 1 Mm, based on the average initial heights of the four observed filament events consisting of two failed and two full eruptions. Many recent studies of full eruptions indicate a
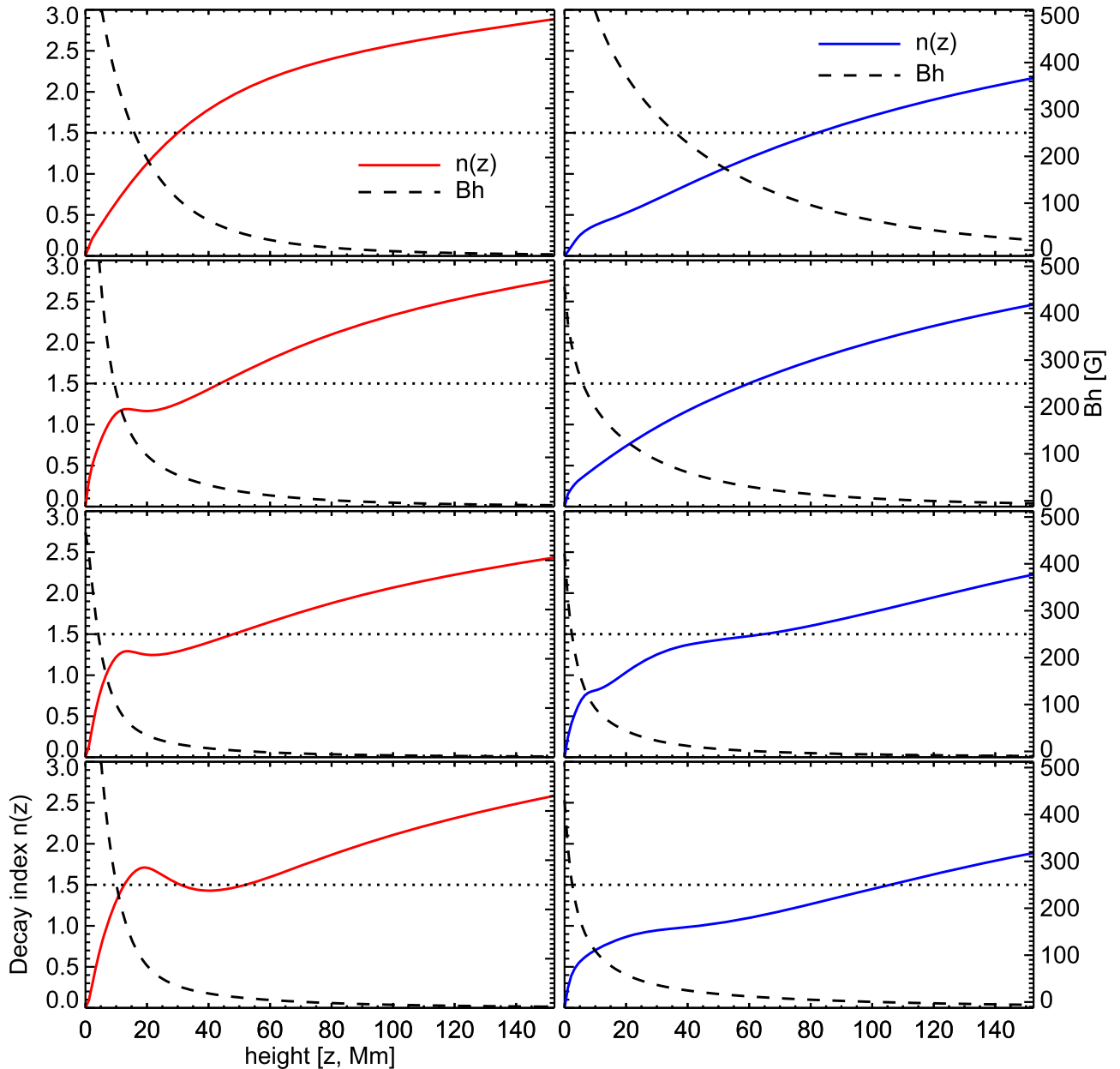
Figure 8. Decay index of background horizontal field strength as a function of height. Left column: typical cases of eruptive flares M4.5, X2.2, X1.0, and X2.1 originating from ARs 12158, 11158, 12017, and 12297 respectively. The critical heights in these events are 30.21 Mm, 42.4 Mm, 40.94 Mm, and 10.96 Mm respectively. Right column: typical cases of confined flares X2.0, M1.1, C5.4, and C6.9 originating from ARs 12192, 12253, 11936, and 12472 respectively. The observed critical heights for these cases are 82.25 Mm, 57.76 Mm, 62.51 Mm, and 103.1 Mm respectively. B_h is also shown on the y-axis scale on the right in each panel. The dotted horizontal line refers to $n_{crit} = 1.5$.

critical height well below 42 Mm (e.g., Cheng et al. 2011; Vemareddy & Zhang 2014; Sun et al. 2015). Based on this segregation of events (vertical dashed line), about 90% (34 of 38) of the eruptive flares have a critical height less than 42 Mm and nearly 70% (27 of 39) of the confined flares have a critical height beyond 42 Mm, as evident in Figure 9. Although the dependency of critical heights varies in individual cases, generally they depend on the strength of the background field confinement but not on the intensity of flares. This indicates that the background field for the confined cases has an extended or stronger confinement than for the eruptive ones. Depending on the extent of this confined environment, the unstable core field (or flux rope) near the main PIL would be suppressed or become a CME and is down to individual cases. From this

statistical study, we propose that a CME is likely from an AR coronal background field where $n(z)$ reaches n_{crit} below 42 Mm.

4. Summary and Discussion

Using HMI vector magnetic field observations, we have studied the relation between degree of magnetic non-potentiality and the observed flare/CME in ARs. Understanding the relation between these properties and establishing a statistically significant link with observed activity is key in flare/CME forecasting models. In this connection, we made a systematic analysis of several non-potential proxies, including the decrease in free magnetic energy, during flares/CMEs of different magnitude. The chosen flare cases originated from 40
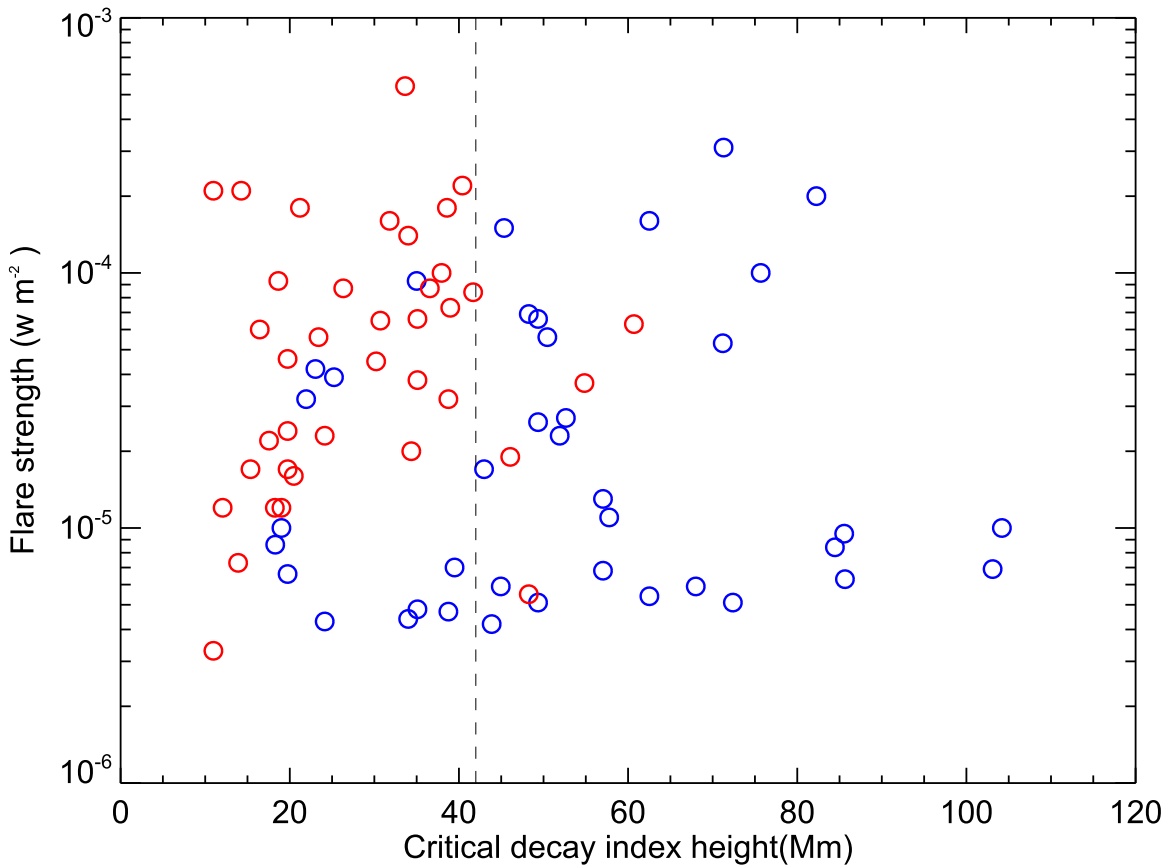
Figure 9. Scatter plot of critical heights for all the flare events in the sample with flare strength. Red (blue) circles represent the eruptive (confined) flares. The vertical dashed line refers to critical height of 42 Mm and divides the eruptive and confined flares.

ARs, of which 83% (19 of 23) in the southern hemisphere and 70% (12 of 17) in the northern hemisphere follow the dominant helicity sign rule (Pevtsov et al. 1995; Bao et al. 2002).

Automatically detected lengths ($SGPIL_A$ and $SSPIL_A$) have a weaker positive correlation with flare strength (CC = 0.40) than manually detected ones ($SGPIL_M$ and $SSPIL_M$). Manual detection accounts for the AIA 1600 Å flare ribbon extension along the PIL. Further, $SGPIL_M$ have a stronger positive correlation with flare strength (CC = 0.9) than do $SSPIL_M$ (CC = 0.8) and therefore the magnetic gradient seems to be better correlated with the intensity of solar flares than magnetic shear. This is in quantitative agreement with Wang et al. (2006) who found this relation in a sample of five X-class flaring ARs.

The total unsigned flux of the entire AR (Φ) and Schrijver's R value were found to be weakly correlated with flare strength but R_{SG}, the total unsigned flux within 15 Mm of $SGPIL_M$, has a statistically significant correlation (0.70). This strong correlation signifies the physical link between the PIL flux and flare intensity. The flux near $SGPIL_M$ must be contributing to the flaring process in a similar way to the flare ribbon reconnection flux defined by Kazachenko et al. (2017). As the amount of flux involved in the flaring process increases, the intensity of flares also increases, but this effect is camouflaged in the Φ and R values and reflects the intensity of the flares. Both $SGPIL_M$ and R_{SG} are related to the actual flux involved in the reconnection along the PIL. Therefore, it is difficult to predict the flare strength a priori based on pre-flare magnetograms, and this points to the missing key aspect in flare prediction models (Mason & Hoeksema 2010).

The total magnetic energy and potential energy of flaring ARs derived from the virial theorem were found to be weakly correlated with flare strength whereas the magnetic free energy derived at the initial timing of flare events has a positive correlation with flare strength. Importantly, the magnetic free energy decreases after the flare eruption and the extent of this decrease has a strong positive correlation with flare strength. These results suggest that there is a strong physical link between the released magnetic free energy and flare productivity, and also the intensity of flares produced. The amount of total magnetic energy and potential energy in an AR are not siignificantly related to the intensity of flares that the AR has produced, but the amount of free energy released provides a major contribution.

We analyzed the dependence of kinematics from our flaring sample that are associated with CMEs. Both $SSPIL_M$ and $SGPIL_M$ are moderately correlated with CME speed. Also, the amount of magnetic free energy decreased during flare eruptions has a relatively strong correlation with CME speed at a CC of 0.56. These findings imply the general relation that the stronger the non-potentiality of the source ARs, larger the CME speed (Wang & Zhang 2007). We also found the most common relation between flare strength and CME speed (CC = 0.49), indicating that faster CMEs tend to be associated with more intense flares.

In addition, the background field appears to be a key factor for a flare to be eruptive. In 90% of eruptive flares, the $n(z)$ curve is steeper, reaching n_{crit} within 42 Mm, whereas >70% confined flares occur in ARs with n_{crit} beyond 42 Mm. Vemareddy (2017) inferred the successive sigmoid formation

and eruption in AR 12371 under slow evolving conditions of predominantly negative helicity flux injection from the SGPIL region. The minimum length of the SGPIL may be the signature of a twisted flux rope. In the confined AR 12192 (no CMEs but with X-flares), the magnetic flux normalized helicity flux is smaller by a factor of 10 and has no signatures of twisted flux rope in coronal imaging observations. As the flux rope is a continuous bundle of twisted field structure, its existence also assumes a continuous SGPIL, but not as small distributed segments. Therefore, the minimum required SGPIL length (31 Mm, Figure 4) and a weak background field ($<$42 Mm) are suggested to be the prime factors for a flare to be eruptive.

The above inference was tested for statistical significance. The skill scores estimated in Section 3.1 suggests that $SGPIL_M$ does not have the ability to accurately predict CMEs from flaring ARs. However, owing to the moderate level of skill scores and correlation with CME productivity (Figure 7(a)), $SGPIL_M$ combined with the measurements of the coronal magnetic field configuration would give better CME predicting capability. These conclusions must be tested with many more events before the relationship can be said to be robust enough to better predict CMEs. Obviously, the next step would be to considering many more events and run a machine learning algorithm. This can learn from input data and improve from experience without human intervention. For our type of study, we can use a nonlinear classification machine learning algorithm, such as the support vector machine algorithm used in Bobra & Couvidat (2015), to enable more quantitative rigour and check for the robustness of the results.

ORCID iDs

N. Vasantharaju https://orcid.org/0000-0003-2336-5208
P. Vemareddy https://orcid.org/0000-0003-4433-8823

References

Abramenko, V. I. 2005, ApJ, 629, 1141
Abramenko, V. I., Wang, T., & Yurchishin, V. B. 1996, SoPh, 168, 75
Alissandrakis, C. E. 1981, A&A, 100, 197
Ambastha, A., Hagyard, M. J., & West, E. A. 1993, SoPh, 148, 277
Bao, S. D., Sakurai, T., & Suematsu, Y. 2002, ApJ, 573, 445
Bloomfield, D. S., Higgins, P. A., McAteer, R. T. J., & Gallagher, P. T. 2012, ApJL, 747, L41
Bobra, M. G., & Couvidat, S. 2015, ApJ, 798, 135
Bokenkamp, N. 2007, PhD thesis, Stanford Univ.
Calabretta, M. R., & Greisen, E. W. 2002, A&A, 395, 1077
Chandrasekhar, S. 1961, Hydrodynamic and Hydromagnetic Stability (Oxford: Clarendon)
Chen, C., Wang, Y., Shen, C., et al. 2011, JGRA, 116, A12108
Cheng, X., Zhang, J., Ding, M. D., Guo, Y., & Su, J. T. 2011, ApJ, 732, 87
Emslie, A. G., Dennis, B. R., Shih, A. Y., et al. 2012, ApJ, 759, 71
Falconer, D. A. 2001, JGR, 106, 25185
Falconer, D. A., Moore, R. L., & Gary, G. A. 2003, JGRA, 108, 1380
Falconer, D. A., Moore, R. L., Porter, J. G., Gary, G. A., & Shimizu, T. 1997, ApJ, 482, 519
Gary, G. A. 1989, ApJS, 69, 323
Georgoulis, M. K., & Rust, D. M. 2007, ApJL, 661, L109
Gopalswamy, N., Yashiro, S., Michalek, G., et al. 2009, EM&P, 104, 295
Guerra, J. A., Park, S.-H., Gallagher, P. T., et al. 2018, SoPh, 293, 9
Guo, J., Zhang, H. Q., & Chumak, O. V. 2007, A&A, 462, 1121
Hagino, M., & Sakurai, T. 2004, PASJ, 56, 831
Hagyard, M. J. 1988, SoPh, 115, 107
Hagyard, M. J., & Rabin, D. M. 1986, AdSpR, 6, 7
Hagyard, M. J., Venkatakrishnan, P., & Smith, J. B., Jr. 1990, ApJS, 73, 159
Hoeksema, J. T., Liu, Y., Hayashi, K., et al. 2014, SoPh, 289, 3483
Jing, J., Song, H., Abramenko, V., Tan, C., & Wang, H. 2006, ApJ, 644, 1273
Jing, J., Tan, C., Yuan, Y., et al. 2010, ApJ, 713, 440
Kazachenko, M. D., Lynch, B. J., Welsch, B. T., & Sun, X. 2017, ApJ, 845, 49
Kosovichev, A. G., & Zharkova, V. V. 2001, ApJL, 550, L105
Leka, K. D., & Barnes, G. 2003a, ApJ, 595, 1277
Leka, K. D., & Barnes, G. 2003b, ApJ, 595, 1296
Leka, K. D., & Barnes, G. 2007, ApJ, 656, 1173
Leka, K. D., Canfield, R. C., McClymont, A. N., et al. 1993, ApJ, 411, 370
Leka, K. D., Canfield, R. C., McClymont, A. N., & van Driel-Gesztelyi, L. 1996, ApJ, 462, 547
Liu, Y. 2008, ApJL, 679, L151
Low, B. C. 1982, SoPh, 77, 43
Mason, J. P., & Hoeksema, J. T. 2010, ApJ, 723, 634
Metcalf, T. R., Leka, K. D., & Mickey, D. L. 2005, ApJL, 623, L53
Molodensky, M. M. 1974, SoPh, 39, 393
Olmedo, O., & Zhang, J. 2010, ApJ, 718, 433
Pevtsov, A. A., Canfield, R. C., & Metcalf, T. R. 1994, ApJL, 425, L117
Pevtsov, A. A., Canfield, R. C., & Metcalf, T. R. 1995, ApJL, 440, L109
Sadykov, V. M., & Kosovichev, A. G. 2017, ApJ, 849, 148
Schou, J., Scherrer, P. H., Bush, R. I., et al. 2012, SoPh, 275, 229
Schrijver, C. J. 2007, ApJL, 655, L117
Schrijver, C. J., De Rosa, M. L., Title, A. M., & Metcalf, T. R. 2005, ApJ, 628, 501
Sharykin, I. N., Sadykov, V. M., Kosovichev, A. G., Vargas-Dominguez, S., & Zimovets, I. V. 2017, ApJ, 840, 84
Song, H., Tan, C., Jing, J., et al. 2009, SoPh, 254, 101
Song, H., Yurchyshyn, V., Yang, G., et al. 2006, SoPh, 238, 141
Su, J. T., Jing, J., Wang, S., Wiegelmann, T., & Wang, H. M. 2014, ApJ, 788, 150
Sun, X. 2013, arXiv:1309.2392
Sun, X., Bobra, M. G., Hoeksema, J. T., et al. 2015, ApJL, 804, L28
Tian, L., Wang, J., & Wu, D. 2002, SoPh, 209, 375
Tiwari, S. K., Venkatakrishnan, P., & Sankarasubramanian, K. 2009, ApJL, 702, L133
Toriumi, S., Schrijver, C. J., Harra, L. K., Hudson, H., & Nagashima, K. 2017, ApJ, 834, 56
Török, T., & Kliem, B. 2005, ApJL, 630, L97
Vemareddy, P. 2017, ApJ, 845, 59
Vemareddy, P., Ambastha, A., & Maurya, R. A. 2012, ApJ, 761, 60
Vemareddy, P., Venkatakrishnan, P., & Karthikreddy, S. 2015, RAA, 15, 1547
Vemareddy, P., & Zhang, J. 2014, ApJ, 797, 80
Wang, H., Ewell, M. W., Jr., Zirin, H., & Ai, G. 1994a, ApJ, 424, 436
Wang, H.-M., Song, H., Jing, J., et al. 2006, ChJAA, 6, 477
Wang, J., Shi, Z., Wang, H., & Lue, Y. 1996, ApJ, 456, 861
Wang, T., Xu, A., & Zhang, H. 1994b, SoPh, 155, 99
Wang, Y., & Zhang, J. 2007, ApJ, 665, 1428
Zhang, H., & Bao, S. 1999, ApJ, 519, 876
Zirin, H., & Wang, H. 1993, SoPh, 144, 37